Optical shrinkage curve characterization as a tool for assessing cyclic wetting-drying effects on hydraulic conductivity of fine-grained soils

Lorenz Spillecke[1*], *Alexander* Knut[1], and *Ralf* Thiele[1]

[1] Institute for Geotechnics Leipzig, Leipzig UAS, Germany

Abstract. Understanding shrinkage behaviour in soft soils is essential for assessing structural and hydraulic stability under environmental stress. This study applies a shrinkage-curve-based method to evaluate soil behaviour before and after cyclic wetting-drying. The main objective is to identify how structural integrity influences shrinkage response and hydraulic sensitivity. Shrinkage curves were generated using a novel high-resolution optical volume measurement system, enabling continuous monitoring of volumetric changes during drying. Hydraulic conductivity and shrinkage tests were performed on representative fine-grained soils exhibiting varying fines contents both prior to and after controlled wetting-drying cycles. The wetting was performed using a capillary suction method, while drying occurred under controlled room temperature conditions, replicating the natural wetting and evaporation processes observed in the field. Derived shrinkage parameters were correlated with hydraulic conductivity before and after 5 wetting-drying cycles. This correlation provides a quantitative link between mechanical deformation and hydraulic evolution across different soil conditions. If changes occur during the residual shrinkage phase, results suggest these may be reflected in more pronounced increases in hydraulic conductivity following consecutive wetting-drying cycles. The post-cyclic shrinkage curves are used to validate these observations, indicating the link between structural degradation and the rise in hydraulic conductivity. These findings emphasize that cyclic wetting-drying induces irreversible changes in density and microstructure. The proposed methodology provides an efficient way to predict post-cyclic soil behaviour, eliminating the need for resource-intensive repeated long-term testing, contributing to improved evaluation and design of hydraulic barriers and other soft soil infrastructures.

1 Introduction

Earthen sealing layers in levees, dams, and embankments constitute critical hydraulic barriers that ensure structural safety and prevent uncontrolled seepage. Projected climate-change scenarios across multiple regions indicate increasingly severe hydrological extremes, characterized by prolonged drought periods alternating with intense precipitation events [1-2]. These conditions subject fine-grained barrier materials to more frequent and more extreme cyclic wetting-drying (W-D) loading, intensifying structural and hydraulic degradation even when protective surface layers are present.

Laboratory investigations have consistently documented substantial increases in saturated hydraulic conductivity following repeated W-D cycles. Some reported changes of one to two orders of magnitude after only a few cycles [2-4]. More recent studies have confirmed these findings [5-7], with some cases showing increases up to three orders of magnitude, representing a 1000-fold change in permeability. The underlying mechanisms driving this degradation include progressive aggregate loosening, micro-crack formation, and attendant reductions in bulk density [6,8-10]. Microstructural analyses utilizing porosimetry and nuclear magnetic resonance confirm that these processes irreversibly alter the pore size distribution, expanding interconnected macropore networks at the expense of smaller pores [11,12]. These structural modifications are influenced by soil-specific factors such as initial fabric [13-15], mineralogy [9,15] and clay content, as well as external conditions including stress state and environmental factors such as root growth [15].

Current German design standards for mineral sealing layers typically prescribe maximum hydraulic conductivity thresholds, commonly $k_f \leq 1 \times 10^{-9}$ m/s and target compaction levels, such as 97% of Standard Proctor density (DWA-M 512-1, 2012). These criteria implicitly assume that material properties remain constant throughout the service life of the structure. However, this static design philosophy does not account for the time-dependent evolution of hydraulic and mechanical properties under recurring hydrological stress. Dense, highly compacted specimens tend to loosen as fissures reopen and aggregate fabric relaxes, whereas initially loose specimens may densify [6]. Consequently, design values derived from static laboratory tests cannot guarantee long-term sealing performance if soil properties evolve under cyclic

* Corresponding author: lorenz.spillecke@htwk-leipzig.de

moisture stress. To transition toward performance-based design frameworks, robust and efficient test methods are required that can characterize the sensitivity of barrier soils to W-D loading and predict their long-term behaviour.

1.1 State of the art in shrinkage testing

Volumetric shrinkage during desiccation represents a fundamental hydro-mechanical process that integrates multiple degradation mechanisms, including structural rearrangement, density loss, and crack initiation [16]. Conventional shrinkage characterization relies primarily on the shrinkage limit test specified in standards such as DIN EN 18122-2, ASTM D4943-18, and BS 1377. The shrinkage limit represents the water content below which no further bulk-volume reduction occurs despite continued drying. However, the standard calculation procedure assumes that the soil remains fully saturated throughout drying until reaching the shrinkage limit, an assumption that has been shown to be frequently violated in practice [17]. This leads to systematic overestimation of the shrinkage limit, with calculated values sometimes exceeding even the plastic limit.

Traditional volume measurement methods present additional challenges. Early shrinkage studies employed intrusive displacement techniques using kerosene or petroleum, which were temperature-sensitive and allowed fluid to enter cracks [18]. Mercury displacement methods, later standardized in ASTM protocols, functioned only on smooth, crack-free specimens and posed serious toxicity hazards. Immersed weighing techniques with wax or saran coatings were safer but slow, introduced mass uncertainties, and risked soil loss during coating removal [19]. Geometric approaches using callipers suffer from irregular specimen shapes and edge effects, while the balloon technique experiences membrane creep [20]. These limitations have motivated the development of non-contact optical measurement methods.

Modern optical measurement techniques enable continuous, high-resolution tracking of the entire soil-shrinkage curve (SSC) throughout the drying process. The SSC describes the relationship between void ratio and moisture ratio and can be decomposed into distinct phases: structural, linear (or proportional), residual, and zero shrinkage [21-23]. Empirical observations across various soil types reveal that not all soils exhibit the complete four-phase pattern, leading to classification of shrinkage curves into six distinct types (A-F) based on which phases are present [21]. Each phase reflects different dominant mechanisms governing soil-water interaction, ranging from air entry and capillary-driven volume loss in the structural and linear phases to physicochemical forces at low moisture contents during the residual phase.

To describe the SSC mathematically, Peng and Horn [23] adapted the inverse of the van Genuchten equation [24], originally developed for soil water retention curves. By evaluating the first and second derivatives of this model, the inflection points delimiting shrinkage regimes can be objectively identified, and a model-based shrinkage limit can be defined at the beginning of the zero-shrinkage phase. This model-based approach consistently yields shrinkage limits at lower water contents than standard methods and aligns more closely with the physical definition of a shrinkage limit.

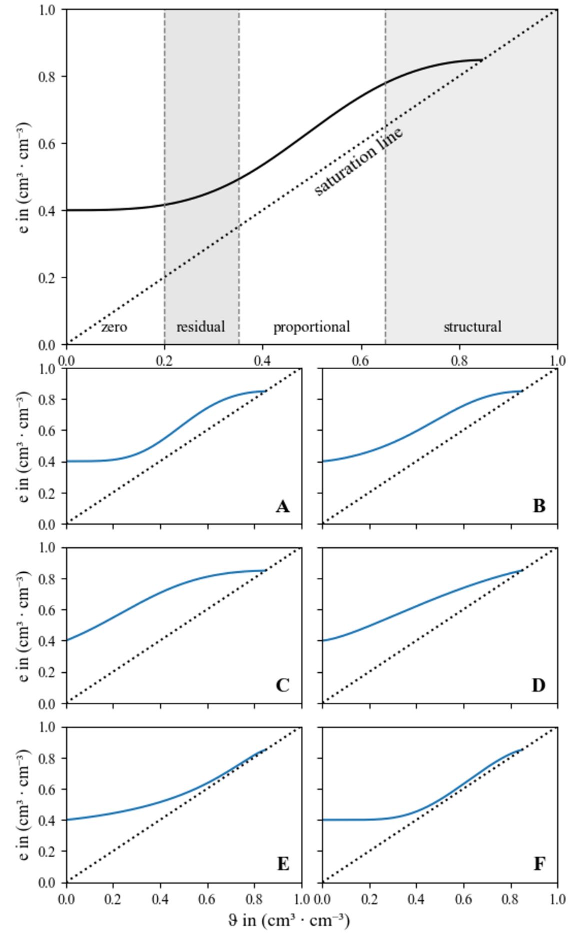

Fig. 1. Qualitative interpretation of shrinkage phases referenced as Types A-F by Peng & Horn [21].

Several non-contact optical techniques have been developed for monitoring volumetric changes during shrinkage. X-ray computed tomography (CT) provides high precision and three-dimensional internal structure visualization [25] but remains expensive and unsuitable for continuous long-term measurements. Three-dimensional laser profilometry has been successfully employed in multiple studies, with rotating-specimen systems, traversing lasers, or hybrid setups consistently reporting submillimetre accuracy [26-31]. Image-based approaches calculate volume from planar area measurements combined with independent height readings or assumptions of isotropic contraction [30]. While less expensive than laser instrumentation, two-dimensional methods generally deliver lower precision due to their reliance on geometric assumptions and limited vertical resolution.

1.2 Linking shrinkage behaviour to cyclic W-D response

Recent research has begun exploring the relationship between shrinkage characteristics and sensitivity to W-D cycling. Coppola et al. (2012) suggested that volumetric shrinkage integrates key phenomena such as structural changes, crack generation, and density loss, and therefore might be closely linked to effects occurring during W-D cycles. While conventional shrinkage-limit tests deliver only a single index value, modern optical methods can trace the entire SSC with submillimetre resolution and thus offer a far richer dataset for material characterization [26-32].

Preliminary correlations suggest that parameters derived from the complete shrinkage curve, particularly characteristics of the residual shrinkage phase, may correlate with post-cyclic changes in hydraulic conductivity. The residual phase represents a critical transition where shrinkage rate declines while mainly hygroscopic water evaporates [22]. During this phase, soils experience high suction stresses that may induce microstructural rearrangements persisting through subsequent wetting cycles. Traditional classification indices, such as plasticity index, grain size distribution, or conventional shrinkage limits, have shown limited predictive capability regarding sensitivity to hydraulic degradation under cyclic loading [33]. This observation is consistent with previous studies emphasizing that hydraulic response under cyclic moisture stress is largely governed by internal structural rearrangements and micro-cracking, which cannot be adequately described by conventional soil indices [34-36].

2 Material and sample preparation

The research utilized four lean clays (CL), one silty clay (CL-ML) and one silt (ML), all categorically allowed for surface barrier applications in levee infrastructure. In accordance with DIN 18122-2 standards, particles exceeding 0.5 mm were removed prior to testing. Six natural soils were selected with slight variations in clay and sand content. These soils are devoid of organic material. A summary of the tested materials is provided in Table 1. The corresponding particle size distribution is shown in Fig. 2.

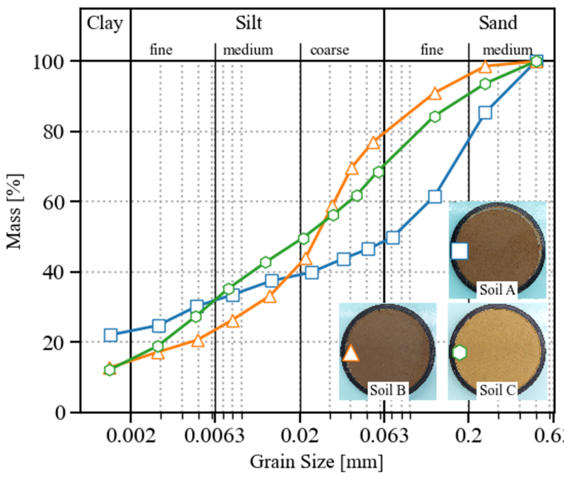

Fig. 2. Particle size distribution of all 6 distinct soil samples. Grain size > 0.5 mm was removed before.

The Atterberg limits were determined following DIN EN ISO 17892-12 standards. The shrinkage limit was measured in accordance with DIN 18122-2, utilizing the calliper method to assess the volume of the dry sample. Particle densities were assumed at 2.68 Mg/m³.

For specimen preparation, the samples were oven dried, grinded and distilled water amounting to 1.1 times the liquid limit (LL) was added to achieve the prescribed remoulding moisture content. Samples were cast into acrylic-glass rings with an internal diameter of 70 mm and a height of 14.15 mm, positioned on an acrylic plate. To facilitate image processing, the ring faces were pre-wrapped with black film, and the plate was wrapped with blue film. Initial mass and geometric dimensions were recorded, and specimens were centrally positioned on balances directly beneath a fixed camera-laser assembly for measurement.

A total of five wetting-drying cycles were conducted, as the most significant microstructural changes typically occur within the initial cycles, after which the soil structure homogenizes and reaches a reversible equilibrium. During these cycles, the re-wetting phase was conducted in two stages to carefully control the microstructural response. Initially, the dried specimens were pre-wetted via vapor absorption in a climate chamber at 35 °C and 95% relative humidity for three days. Following this, the specimens were placed on a permeable plate in a water bath to allow liquid water infiltration via capillary suction, leading to saturation and slight swelling above the ring geometry. Although it was not possible to determine the wetting rate, saturation occurred after estimated 1 to 3 hours.

3 Methods

3.1 Mass and volume measurements

Fig. 3a shows the experimental setup, which included a Raspberry Pi camera (1/2.3-inch sensor, 12-megapixel resolution, 16 mm telephoto lens) mounted on a linear movable rig in a shaded room.

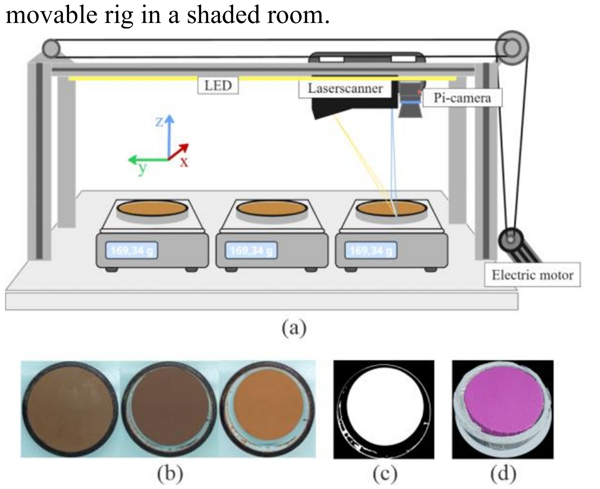

Fig. 3. (a) Experimental setup, (b) image of a sample at beginning, after 24 hours and after 48 hours, (c) thresholded image and (d) 3d model.

Digital images were captured at 30-minute intervals throughout the desiccation process. Surface topography was simultaneously acquired using a 2D laser profilometer (Keyence LJ-X8300) with a planar resolution of 0.1 mm and vertical resolution of 3 µm.

For estimation of the SSC, it is necessary to determine the sample volume and mass during the shrinkage process. Mass measurements were automatically recorded every 10 minutes. The ambient temperature was maintained at 22°C throughout all experiments.

Each experimental cycle was terminated when no significant mass change was observed, typically after 3 to 4 days, at which point specimens usually retained approximately 2% residual moisture by weight. Subsequently, specimens were oven-dried at 60°C until reaching constant mass. Final residual volume was assessed through laser scanning with calliper validation.

3.2 Volume determination

3.2.1 Data pre-processing and sample detection

Raw sensor data were stored in HDF5 format containing synchronized luminance (brightness) and height arrays. These arrays were extracted and pre-processed through a parallelized pipeline. Height maps underwent threshold filtering with empirically determined bounds followed by remapping to maximize dynamic range.
Because three samples were scanned in a single scan, each image sequence was partitioned into three sub-regions. For each sub-region, cropping parameters were calculated based on the brightness centroid of the luminance image to prepare a squared and centred image of luminance and height each.

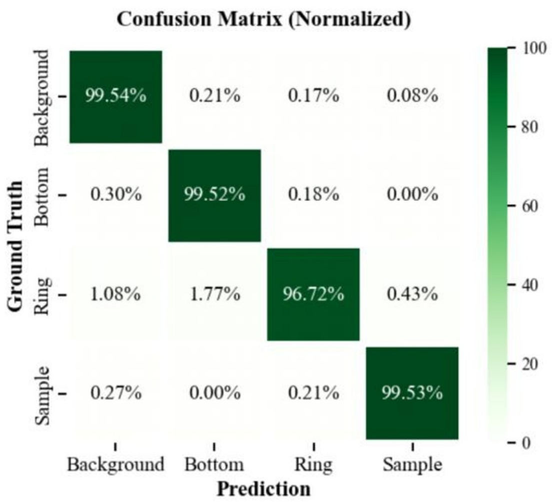

(a)

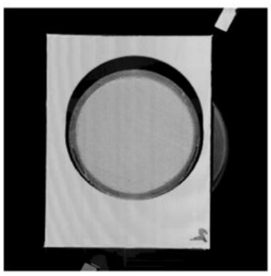

(b)

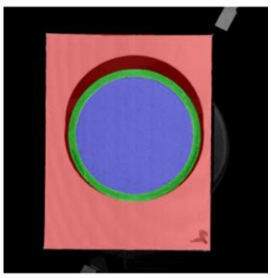

(c)

Fig. 4. (a) Reliability display of sample masking, (b) luminance/brightness image result of a laser scan, (c) mask overlay on top of image.

Sample segmentation was performed using a U-Net++ architecture with an EfficientNet-B3 encoder pre-trained on ImageNet, adapted for dual-channel input (luminance and height). The decoder produced pixel-wise classification into background, bottom surface, ring structure, and soil sample (Fig. 4c). Training was conducted on 114 manually annotated image pairs (70% training, 15% validation, 15% testing) using a combined focal and Dice loss function. The focal loss was employed to address class imbalance in the segmentation task, as background pixels significantly outnumber for example ring pixels. The overall accuracy of the process is shown in Fig. 4a, where the correlation matrix which especially matters regarding sample recognition performs by masking 99.53% of the pixels belonging to the sample correctly.

3.2.2 Post-processing and outlier removal

To improve segmentation robustness, a histogram-based statistical filter was applied to remove measurement artifacts. Standard deviation was estimated from the central 68% of the distribution to minimize influence from outliers. Pixels deviating beyond class-specific thresholds (Bottom: 2σ, Ring: 1.5σ, Sample: 2.8σ) were classified as outliers.

The laser produces measurement outliers frequently near edge regions by design. Pixels classified as outliers near the edge region of the sample were removed. Outliers within the sample were filled with the median height value of the statistically validated sample region to preserve geometric continuity.

3.2.3 Volume calculation and calibration

Sample volume was determined through calibrated height-to-metric conversion. The median height difference between ring top and bottom surface provided internal calibration:

$$k_{vertical} = \frac{h_{ref}}{z_{ring} - z_{bottom}} \tag{1}$$

where $h_{\mathrm{ref}} = 14.15$ mm is the known ring height, and z_{ring} and z_{bottom} are the respective median pixel intensities in 16-bit depth. Horizontal calibration was set to 0.05 mm/pixel based on reference geometry and previous calibration. Sample heights were calculated as:

$$h_{\mathrm{sample}}(x,y) = \left(z_{\mathrm{sample}}(x,y) - z_{\mathrm{bottom}}\right) \cdot k_{\mathrm{vertical}} \tag{2}$$

for all pixels (x, y) classified as sample. Total volume was obtained by:

$$\mathrm{V_i} = \sum\nolimits_{(x,y)\,\in\,\mathrm{sample}} h_{sample}(x,y) \cdot A_{pixel} \tag{3}$$

where $A_{\mathrm{pixel}} = 0.0025$ mm² is the pixel area. The void ratio was determined according to:

$$e_i = V_i \frac{\varrho_s}{m_d} - 1 \tag{4}$$

The time-resolved void ratios were paired with the corresponding mass change of the samples $\Delta\, m_i$ to construct shrinkage curves in the $e(\vartheta)$space, whereas the moisture ratio is defined as:

$$\vartheta_i = \frac{V_{w,i}}{V_s} = \frac{\varrho_s\left(m_{f,0} - \Delta\, m_i\right)}{\varrho_w\, m_d} \qquad (5)$$

within Equation (5) a constant density of the pore water of $\varrho_w = 1\ g/cm^3$ is assumed. The initial dry and wet mass m_d, m_w are known due to the sample preparation.

3.3 Saturated hydraulic conductivity: Sample preparation and W-D cycles

Samples were prepared in 250 ml cylinders (Fig. 5a) at optimal water content using multilayer compaction to 97% of Proctor density, following the design criteria of DWA-M 512-1 (2012). Saturation was achieved by capillary suction in a basin and considered complete once the mass change rate fell below 0.5 g/day. Although capillary suction may not fully saturate samples [36], it was assumed that full saturation is not essential, as most relevant property changes are expected to occur above the air entry point.

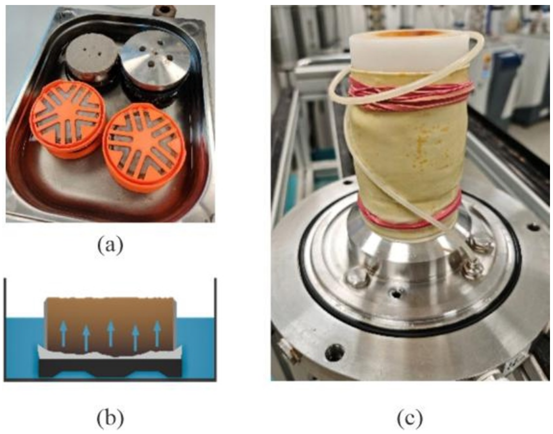

Fig. 5. (a) saturation method by capillary suction, (b) schematic display of saturation method, (c) prepared hydraulic conductivity measurement sample in triaxial cell.

After each drying cycle, samples were re-saturated following the same procedure, with the process repeated over five cycles to minimize sample disturbance. Hydraulic conductivity was measured after the fifth cycle in a triaxial cell in accordance with DIN EN ISO 17892-11 (2021), applying a backpressure of 800 kPa to achieve full saturation and a uniform hydraulic gradient across all samples. To avoid structural alteration from backpressure saturation, separate samples were used for measurements after preparation and after five W-D cycles.

4 Results

4.1 Shrinkage behaviour during cyclic wetting-drying

The soil-shrinkage curves (SSCs) for the first cycle, following sample preparation at water content at 1.1 times of the liquid limit are displayed in Fig. 6-WD1, and the results for the SSCs across following wetting-drying cycles are found in the remaining graphs of Fig. 6. Each soil is represented by its respective colour.

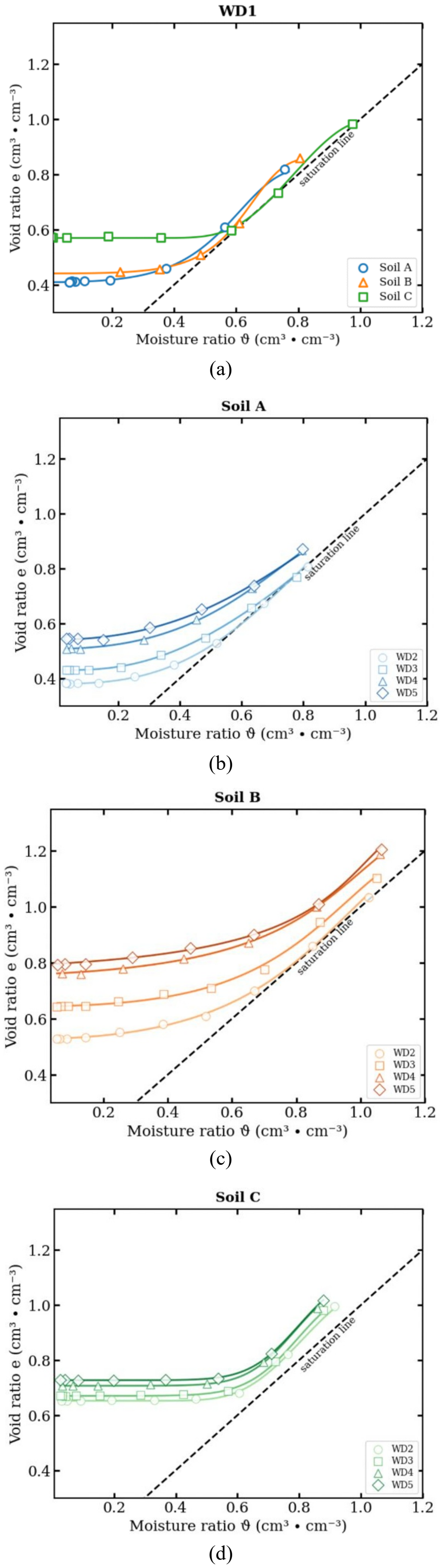

Fig. 6. Soil Shrinkage Curves (SSC). WD1 depicts the initial state after sample preparation (a), followed by consecutive cycles for each soil (b-d). The graphs plot void ratio e versus moisture ratio ϑ, with the dashed line indicating full saturation.

The displayed curve was fitted by applying the Peng & Horn model:

$$e(\upsilon) = e_r + \frac{e_s - e_r}{\left(1 + \left(\frac{\alpha \cdot \vartheta}{e_s - \vartheta}\right)^{-n}\right)^m} \quad (6)$$

within this e_r and e_s are the residual and saturated void ratio and α, m and n are fitting parameters. The data point markers are visible for each 20th measurement, however the curve fit along the applied model included all data points.

4.1.1 Evolution of shrinkage curves across cycles

All three soils exhibited a progressive upward shift of the shrinkage curves from WD2 to WD5, indicating systematic volumetric expansion between cycles. This trajectory suggests incomplete recovery during re-saturation or residual structural loosening.

Soil A demonstrated clear changes along wetting-drying cycles, with shrinkage curves shifting upward from WD2 (initial saturated void ratio $e_0 \approx 0.76$) to WD5 ($e_0 \approx 0.88$). The structural shrinkage phase was less pronounced compared to Soil B and C.

Soil B displayed the most pronounced cyclic evolution, with an increase in void ratio of almost 40% (at dry state). However, the zero-shrinkage phase does not seem apparent for this soil type. The shrinkage curves shifted markedly upward from WD2 to WD5, with structural changes being particularly distinct.

Soil C also exhibited a progressive upward shift and scaling of the shrinkage curves, with void ratios increasing from approximately 0.65 at the dry state in WD2 to 0.75 in WD5, while the increase at all phases was less pronounced. The proportional shrinkage phase maintained a consistent gradient across all cycles, followed by a smooth transition into the residual and zero shrinkage phase.

4.1.2 Phase-specific characteristics

All three soils exhibited Type E or Type F shrinkage behaviour according to the Peng & Horn [21] classification. The structural shrinkage phase, characterized by minimal void ratio reduction despite significant moisture loss was not established in any of the samples and the zero shrinkage is only clearly distinguished in soil C.

The proportional shrinkage phase, where void ratio decreases equally to moisture ratio, displayed varying gradients across soil types. Soil B and C showed gradients sometimes exceeding 45 degrees.

4.2 Hydraulic conductivity

Fig. 7 presents the measured saturated hydraulic conductivity for the investigated soil samples. Here, k_f^0 denotes the initial hydraulic conductivity, while k_f^5 represents the hydraulic conductivity after five wetting–drying (W–D) cycles. For all soils, the initial conductivity is lower than the value measured after five consecutive W–D cycles. The magnitude of this increase differs markedly between soils: Soil C shows a 3.6-fold increase, whereas Soil A exhibits an almost 200-fold increase.

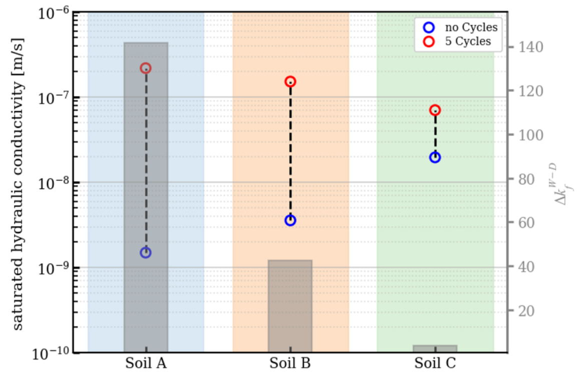

Fig. 7. Hydraulic conductivities before and after WD-cycles, measured according to DIN EN ISO 17892-11 2021.

To quantify how sensitive a given soil is to W–D-induced changes in hydraulic conductivity, the following metric is used:

$$\Delta k_f^{W-D} = \frac{k_f^5}{k_f^0} \quad (7)$$

Equation (7) expresses the absolute change in hydraulic conductivity.

4.3 Implications for cyclic sensitivity

The systematic upward shift of shrinkage curves with increasing cycle number suggests structural modifications. Fig. 8 illustrates the evolution of the residual phase dimensions in moisture ratio, and moisture ratio at $w_s\ at\ \frac{de}{d\vartheta} = 0.2$ across five cycles for three soil compositions. The residual phase provides constant results regarding its length but shifts along the moisture ratio range. The values for $w_s\ at\ \frac{de}{d\vartheta} = 0.2$ display an upward trend for soil B but constant for the other soils.

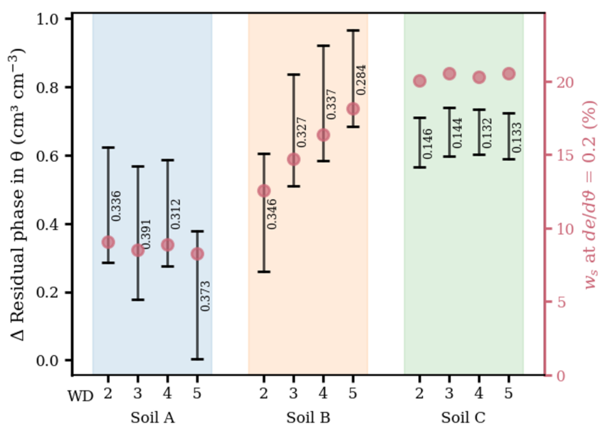

Fig. 8. Correlation overview, length of residual phase on the left side, shrinkage limit at characteristic $w_s\ at\ \frac{de}{d\vartheta} = 0.2$ on the right side.

5 Discussion

The upward shift of shrinkage curves with increasing cycle number confirms progressive and irreversible structural modifications in fine-grained soils. Each successive wetting-drying cycle increased void ratios at both saturated and dry states, indicating incomplete volumetric recovery during rewetting and accumulation of structural damage. This systematic increase in void ratio at both saturated and dry states can be physically interpreted as the progressive generation of macropores and inter-aggregate fissures. This interpretation is supported by studies, which demonstrate that cyclic moisture variations irreversibly shift the internal pore-size distribution toward a macropore-dominated state [11, 12]. This behaviour also aligns with established mechanisms where W-D cycling causes aggregate loosening, microcrack formation, pore network reorganization and bulk density reduction [6, 8-10]. Consequently, the massive increases in saturated hydraulic conductivity observed in this study (up to a 200-fold increase in Soil A) are likely a direct macroscopic consequence of this enhanced macropore volume and connectivity.

The residual shrinkage phase may induce particle rearrangement and interaggregate bonding changes through high suction stresses that persist through subsequent cycles [31-32]. Shrinkage-curve descriptors including residual-phase width and overall curve shape demonstrated consistent, soil-specific signatures across specimens, confirming their reliability as intrinsic material characteristics. While these differences might visually suggest a correlation with the varying clay content of this limited subset, particle size distribution alone is insufficient to fully govern the cyclic shrinkage sensitivity, which is heavily superimposed by initial fabric and mineralogy. However, correlations between these descriptors and post-cyclic hydraulic conductivity changes weakened over successive wetting–drying cycles, suggesting that macrostructural processes such as fissure formation and crack network development under unconfined free-swelling conditions increasingly dominate hydraulic response.

6 Conclusion

This study presents an optical framework for characterising shrinkage behaviour of fine-grained soils under cyclic wetting–drying, combining laser profilometry, image-based area detection and machine-learning segmentation to obtain continuous, non-destructive volume data throughout drying. The method generates complete soil shrinkage curves with high temporal resolution, enabling observation of curve evolution after repeated environmental loading. With a total test duration of approximately four to five days for three specimen and a fully automated data acquisition pipeline, the method enables systematic studies across multiple soil types and influencing factors, allowing large numbers of shrinkage curves to be evaluated in a shorter time than similar approaches.

The experimental results show a systematic upward shift of shrinkage curves with increasing cycle number, indicating progressive and irreversible structural alteration consistent with porosity increase and fabric loosening.

The consistent shape of the residual shrinkage phase across cycles demonstrates it as being a robust soil-specific characteristic, reflecting stable microstructural retention behaviour even under repeated wetting–drying.

Furthermore, while macrostructural crack development and pore reorganization dominate the hydraulic degradation under unconstrained laboratory conditions, establishing reliable predictions for field applications like levee cores requires future testing under representative confining stresses to restrict lateral swelling.

From an application perspective, the approach may complement time-consuming cyclic hydraulic testing by providing shrinkage descriptors with higher information density per test. Development of a robust framework for continued assessment requires several further steps: reducing uncertainty from the underside assumption (e.g., dual-side measurement), systematic testing under surcharge to simulate levee stress conditions, and integration of suction-controlled measurements with microstructural methods (ESEM/MIP) to establish links between shrinkage-curve features, pore-network changes and flow-relevant defects.

References

1. A. Puppala, A. Cerato, Heave distress problems in chemically-treated sulfate-laden materials. Geo-Strata **10**, 28-32 (2009).
2. J.K. Janga, K.R. Reddy, J. Schulenberg, Climate change impacts on safety of levees: A review / Impacts du changement climatique sur la securité des digues: un examen. Proc. ECSMGE 2024 (2024). https://doi.org/10.1201/9781003431749-310
3. L.C. Lin, C.H. Benson, Effect of wet–dry cycling on swelling and hydraulic conductivity of GCLs. J. Geotech. Geoenviron. Eng. **126**, 40-49 (2000). https://doi.org/10.1061/(ASCE)1090-0241(2000)126:1(40)
4. K.S.S. Rao, S.M. Rao, S. Gangadhara, The impact of cyclic wetting and drying on the swelling behaviour of stabilized expansive soils. Eng. Geol. **60**, 223-233 (2001). https://doi.org/10.1016/S0013-7952(00)00089-3
5. H. Lu, J. Liu, Y. Li, Y. Dong, Heat transport and water permeability during cracking of the landfill compacted clay cover. Int. J. Geophys. **2015**, 786419 (2015). https://doi.org/10.1155/2015/786419
6. F. Louati, H. Trabelsi, J. Mehrez, et al., Wet–dry cycles effect on the saturated hydraulic conductivity. Eur. J. Environ. Civ. Eng. **25**, 1079-1098 (2018). https://doi.org/10.1080/19648189.2018.1541144
7. M. De Camillis, G. Di Emidio, A. Bezuijen, R.D. Verastegui-Flores, Hydraulic conductivity of modified bentonites after wet and dry cycles (2019). https://doi.org/10.1007/978-981-13-2224-2_58
8. J. Ivoke, M.S. Khan, et al., Unsaturated hydraulic conductivity variation measurements in expansive clay during seasonal fluctuations. Transp. Res. Rec. **2675**,

663-673 (2021). https://doi.org/10.1177/03611981211011994

9. Z. Han, W.-L. Zou, K.-W. Fan, J. Zhang, H. Rahardjo, D.G. Fredlund, Influences of temperature and moisture fluctuations on soil shrinkage and water retention curves of compacted expansive soils. Eng. Geol. **306**, 106533 (2022). https://doi.org/10.1016/j.enggeo.2022.106533
10. M.F. Abbas, A.A. Shaker, M.A. Al-Shamrani, Hydraulic and volume change behaviors of compacted highly expansive soil under cyclic wetting and drying. J. Rock Mech. Geotech. Eng. **15**, 486-499 (2023). https://doi.org/10.1016/j.jrmge.2022.05.015
11. T. Ma, C. Wei, C. Yao, P. Yi, Microstructural evolution of expansive clay during drying–wetting cycle. Acta Geotech. **15**(8), 2355–2366 (2020). https://doi.org/10.1007/s11440-020-00938-4
12. X. Xu, D. Liu, Z. Xian, F. Yang, W. Jian, X. Xu, J. Huang, Influence of Drying–Wetting Cycles on the Water Retention and Microstructure of Residual Soil. Geofluids, 1–15 (2022). https://doi.org/10.1155/2022/9948658
13. A.-N. Zhou, D. Sheng, J.P. Carter, Modelling the effect of initial density on soil-water characteristic curves. Géotechnique **62**, 669-680 (2012). https://doi.org/10.1680/geot.10.P.120
14. A.R. Estabragh, B. Parsaei, A.A. Javadi, Laboratory investigation of the effect of cyclic wetting and drying on the behaviour of an expansive soil. Soils Found. **55**, 304-314 (2015). https://doi.org/10.1016/j.sandf.2015.02.007
15. C.-S. Tang, C. Zhu, Q. Cheng, H. Zeng, J.-J. Xu, B.-G. Tian, B. Shi, Desiccation cracking of soils: A review of investigation approaches, underlying mechanisms, and influencing factors. Earth-Sci. Rev. **216**, 103586 (2021). https://doi.org/10.1016/j.earscirev.2021.103586
16. A. Coppola, H.H. Gerke, A. Comegna, A. Basile, V. Comegna, Dual-permeability model for flow in shrinking soil with dominant horizontal deformation. Water Resour. Res. **48**, W08527 (2012). https://doi.org/10.1029/2011WR011376
17. N. Vogt, E. Birle, D. Heyer, A. Etz, Entwicklung einer neuen Versuchstechnik zur Bestimmung der Grenze zwischen halbfestem und festem Boden, (Bundesanstalt für Straßenwesen Straßenbau, Bergisch Gladbach, 2013). ISBN: 9783956060106
18. D.S. McIntyre, G.B. Stirk, A method for determination of apparent density of soil aggregates. Aust. J. Agric. Res. **5**, 291-296 (1954). https://doi.org/10.1071/ar9540291
19. J.W. Sibley, D.J. Williams, A procedure for determining volumetric shrinkage of an unsaturated soil. Geotech. Test. J. **12**, 181-185 (1989). https://doi.org/10.1520/GTJ10966J
20. A. Tariq, D.S. Durnford, Soil volumetric shrinkage measurements: A simple method. Soil Sci. **155**, 325-330 (1993). https://doi.org/10.1097/00010694-199305000-00003
21. X. Peng, R. Horn, Identifying six types of soil shrinkage curves from a large set of experimental data. Soil Sci. Soc. Am. J. **77**, 377-386 (2013). https://doi.org/10.2136/sssaj2011.0422
22. A.R. Mitchell, Soil surface shrinkage to estimate profile soil water. Irrig. Sci. **12**, 1-6 (1991). https://doi.org/10.1007/BF00190702
23. X. Peng, R. Horn, Anisotropic shrinkage and swelling of some organic and inorganic soils. Eur. J. Soil Sci. **58**, 98-107 (2007). https://doi.org/10.1111/j.1365-2389.2006.00808.x
24. M.Th. Van Genuchten, A closed-form equation for predicting the hydraulic conductivity of unsaturated soils. Soil Sci. Soc. Am. J. **44**, 892-898 (1980). https://doi.org/10.2136/sssaj1980.03615995004400050002x
25. R.L. Mokwa, S.T. Nielsen, X-ray computed tomography for soil testing. Geotech. Test. J. **29**, 398-405 (2006).
26. T. Sander, H.H. Gerke, Noncontact shrinkage curve determination for soil clods and aggregates by three-dimensional optical scanning. Soil Sci. Soc. Am. J. **71**, 1448-1451 (2007). https://doi.org/10.2136/sssaj2006.0372
27. S. Jain, Y.H. Wang, D.G. Fredlund, Non-contact sensing system to measure specimen volume during shrinkage test. Geotech. Test. J. **38**, 403-412 (2015). https://doi.org/10.1520/GTJ20140274
28. J.M. Wong, D. Elwood, D.G. Fredlund, Use of a three-dimensional scanner for shrinkage curve tests. Can. Geotech. J. **56**, 125-132 (2019). https://doi.org/10.1139/cgj-2017-0700
29. B.R. Lexmond, B. van Dam, C.V. Hockin, G. Erkens, J. Griffioen, E. Stouthamer, Measuring shrinkage of expansive soils using a novel automated high-frequency setup. Soil Sci. Soc. Am. J. **88**, 2343-2352 (2024). https://doi.org/10.1002/saj2.20755
30. A.C. Amenuvor, G. Li, J. Wu, Y. Hou, W. Chen, An image-based method for quick measurement of the soil shrinkage characteristics curve of soil slurry. Geoderma **354**, 114165 (2020). https://doi.org/10.1016/j.geoderma.2019.114165
31. S. Henke, A. Vogel, K. Reiswig, Untersuchungen zum Schrumpfverhalten bindiger Böden unter Nutzung von 3D-Laserscanning (2023).
32. A.G. Sharanya, H. Mudavath, T. Thyagaraj, Review of methods for predicting soil volume change induced by shrinkage. Innov. Infrastruct. Solut. **6**, 130 (2021). https://doi.org/10.1007/s41062-021-00485-1
33. D. Izdebska-Mucha, E. Wójcik, Testing shrinkage factors: Comparison of methods and correlation with index properties of soils. Bull. Eng. Geol. Environ. **72**, 15-24 (2013). https://doi.org/10.1007/s10064-012-0449-0
34. B.A. Albrecht, C.H. Benson, Effect of desiccation on compacted natural clays. J. Geotech. Geoenviron. Eng. **127**, 67-75 (2001). https://doi.org/10.1061/(ASCE)1090-0241(2001)127:1(67)
35. E. Romero, P.H. Simms, Microstructure investigation in unsaturated soils: A review with special attention to contribution of mercury intrusion porosimetry and environmental scanning electron microscopy. Geotech. Geol. Eng. **26**, 705-727 (2008). https://doi.org/10.1007/s10706-008-9204-5
36. B.L. Kutter, Effects of capillary number, Bond number, and gas solubility on water saturation of sand specimens. Can. Geotech. J. **50**, 133-144 (2013). https://doi.org/10.1139/cgj-2011-0250